

Infrared spectroscopy of the 2022 eruption of the recurrent nova U Sco

A. Evans^{1*}, D. P. K. Banerjee², C. E. Woodward^{3†}, T. R. Geballe⁴, R. D. Gehrz³, K. L. Page⁵, S. Starrfield⁶

¹*Astrophysics Group, Lennard Jones Laboratory, Keele University, Keele, Staffordshire, ST5 5BG, UK*

²*Physical Research Laboratory, Navrangpura, Ahmedabad, Gujarat 380009, India*

³*Minnesota Institute for Astrophysics, School of Physics & Astronomy, 116 Church Street SE, University of Minnesota, Minneapolis, MN 55455, USA*

⁴*Gemini Observatory/NSF's NOIRLab, 670 N. Aohoku Place, Hilo, HI, 96720, USA*

⁵*School of Physics and Astronomy, University of Leicester, University Road, Leicester, LE1 7RH, UK*

⁶*School of Earth and Space Exploration, Arizona State University, Box 871404, Tempe, AZ 85287-6004, USA*

Accepted XXX. Received YYY; in original form ZZZ

ABSTRACT

We present near-infrared spectroscopy of the 2022 eruption of the recurrent nova U Sco, over the period from 5.2 to 45.4 days after outburst. This is the most intensive infrared study of this nova. Our observations started early after the outburst and extended almost to the end of the “Super Soft” X-ray phase. A major find is the presence of coronal lines from day 9.41, one of the earliest appearances of these in any nova, classical or recurrent. The temperature of the coronal gas is 7×10^5 K. There is also evidence for the presence of much cooler ($\lesssim 2.5 \times 10^4$ K) gas. Remarkable changes are seen in the He I 1.083 μm line, the strength of which declines, then recovers, in anti-correlation with the X-ray behaviour. We conclude that shock ionisation is the dominant excitation mechanism for the coronal line emission. There is evidence in the infrared spectra for the presence of black body emission at ~ 20000 K, which we tentatively identify with the irradiated secondary, and for free-free/free-bound emission. For the previously determined binary inclination of $82^\circ.7$, the implied ejection velocities are as high as 22000 km s^{-1} . These velocities appear unprecedented in nova outflows, and are comparable to those seen in supernovae, thereby marking U Sco as a truly remarkable object.

Key words: stars: individual: U Sco — novae, cataclysmic variables — infrared: stars

1 INTRODUCTION

Recurrent novae (RNe) are a subset of the cataclysmic variable binary systems in which a cool component (the secondary) transfers matter via an accretion disk (AD) onto a white dwarf (WD; the primary). The base of the layer accreted on the WD becomes degenerate, and eventually hot enough to initiate a thermonuclear runaway, resulting in a nova eruption. In time, accretion resumes and eventually another eruption occurs. All novae are recurrent but the erup-

tions of RNe repeat on timescales $\lesssim 100$ yr (see Anupama 2008, for a review).

2 U Sco: NATURE AND RECENT ERUPTIONS

2.1 The binary

U Sco is the most frequent eruptor of the known Galactic RNe. It is known to have undergone eruptions in 1863, (1873, 1884, 1894), 1906, 1917, (1927), 1936, 1945, (1955), 1969, 1979, 1987, 1999, 2010 (2016) (dates in brackets are probable eruptions; see Darnley 2021; Schaefer 2022). U Sco is an eclipsing binary, consisting of a $1.55 \pm 0.24 M_\odot$ WD and a $0.88 \pm 0.17 M_\odot$ secondary; its inclination is $i = 82^\circ.7 \pm 2^\circ.9$ (Thoroughgood et al. 2001). The orbital period prior to the 2022 eruption was 1.2305658 ± 0.0000041 days, as measured

* E-mail: a.evans@keele.ac.uk

† Visiting Astronomer at the Infrared Telescope Facility, which is operated by the University of Hawaii under contract 80HQTR19D0030 with the National Aeronautics and Space Administration.

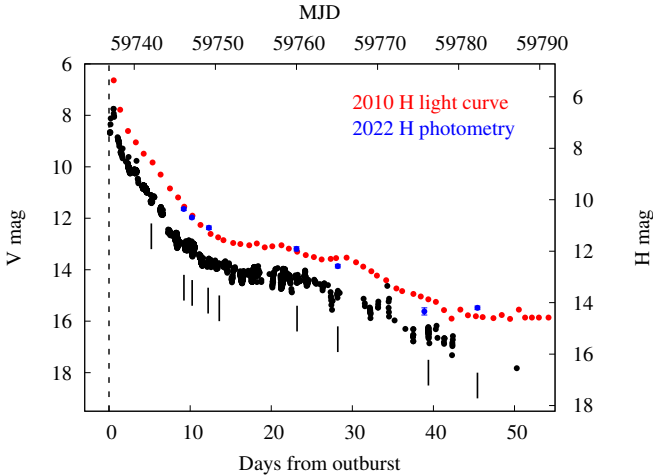


Figure 1. Black points: V band light curve of 2022 eruption; AAVSO data¹. The dashed vertical line indicates the assumed time origin, MJD 59736.72 (see text). Times of the observations described here are indicated by short vertical lines. Red points: H band light curve of the 2010 eruption (Pagnotta et al. 2015). Blue points: H photometry as described in text for the 2022 eruption.

from 2016.78 (the time of the putative 2016 eruption) to 2022.4 (Schaefer 2022). Schaefer also found an increase of 22.4 parts-per-million in the orbital period across the 2010 eruption, concluding that the period change is most likely due to the reaction of the binary to the asymmetric ejection of material during the nova eruption.

While the uncertainty is relatively large, the mass of the WD in U Sco seems uncomfortably high, although the mass limit for differentially rotating white dwarfs can be as high as $4M_{\odot}$, i.e., far higher than the canonical Chandrasekhar limit (e.g., Yoon & Langer 2005). Hachisu et al. (2000) modelled the light curve from the 1999 eruption, and found a WD mass of $1.37 \pm 0.01 M_{\odot}$, very close to that found by Shara et al. (2018) on the basis of modelling the eruptions of classical and RNe. We assume $1.37 M_{\odot}$ here. The secondary star is a sub-giant of spectral type K2 (Anupama 2008). Therefore, unlike RN systems such as RS Oph, in which the secondary is a red giant with a strong wind, the secondary in U Sco is evolved but has little or no wind. For this reason the evolution of an eruption in U Sco is expected to differ significantly from that in a RN system with a giant secondary.

There is evidence that less mass is ejected during an eruption of U Sco than is accreted by the WD between outbursts (Kahabka et al. 1999), suggesting that the WD mass in U Sco is increasing. As the WD likely has CO composition (Mason 2013), U Sco is a candidate Type Ia supernova progenitor (Starrfield et al. 2020).

The distance of U Sco is poorly constrained (Schaefer 2010), but is known to be large, between ~ 8.5 kpc and ~ 15.4 kpc. Where we need to use a distance here, we use 10 kpc.

2.2 A brief summary of three recent eruptions

The 1979 eruption of U Sco was observed at ultraviolet wavelengths by Williams et al. (1981), and at optical and ultraviolet wavelengths by Barlow et al. (1981). While both

studies noted the presence of high ionisation states, such as C IV, N V, O IV, O VI, they did not report any forbidden lines. Indeed, Anupama (2008) stated that, up until the 1999 eruption, no forbidden lines had been reported during outburst. Barlow et al. and Williams et al. also estimated that the ejecta mass was low, $\sim 10^{-7} M_{\odot}$, and that there was evidence for an overabundance of He relative to H.

The 1999 eruption was observed in the optical by Munari et al. (1999). These authors reported a narrowing of $H\alpha$, implying a deceleration of $\sim 270 \text{ km s}^{-1} \text{ day}^{-1}$, and an increase in the degree of ionisation as the eruption progressed. Anupama et al. (2013) found short-term spectral variations during the 2010 eruption, and reported intrinsic linear polarisation due to electron scattering from the disc and jets. They estimated the mass of ejected hydrogen was $\sim 4.6 \times 10^{-6} M_{\odot}$. Maxwell et al. (2012) determined that the helium abundance in the ejecta was not significantly different from solar, in contrast to previous estimates, which had $N(\text{He})/N(\text{H})$ ranging from 0.16 to 4.5 (Evans et al. 2001; Iijima 2002). In an erratum, Maxwell et al. (2015) gave $N(\text{He})/N(\text{H}) = 0.117 \pm 0.014$. All post-1979 eruptions have been characterised by high ejection velocities ($\sim 10000 \text{ km s}^{-1}$; e.g., Barlow et al. 1981; Williams et al. 1981; Iijima 2002; Anupama et al. 2013).

Drake & Orlando (2010) carried out 3-dimensional hydrodynamic simulations of the 2010 eruption. They found that, as the ejecta encountered the secondary star, the secondary gave rise to a “bow shock”, in which the ejecta were shocked to a temperature of a few $\times 10^5$ K. They further concluded that high wind and equatorial gas densities result in X-ray emission that exceeded the observational upper limits, and that the circumstellar gas density is therefore rather low. Hachisu et al. (2000) modelled the light curve of the 1999 eruption, and concluded that the “burning” phase of the eruption, which is accompanied by a strong wind, persisted for the first ~ 20 days of the eruption. In this case one might expect the bow shock associated with the secondary to persist for that length of time.

Near-infrared (NIR) observations were obtained during the eruptions of 1999 (Evans et al. 2001) and 2010 (Banerjee et al. 2010; Mason et al. 2012; Maxwell et al. 2012; Rudy et al. 2022). Evans et al. (2001) noted the presence of an excess in the continuum, which they attributed to free-free emission. Evans et al. reported that there were no coronal lines in the 1999 eruption spectrum, but it is likely that the strong line at $\sim 2.05 \mu\text{m}$ in their data was [AlIX] $\lambda = 2.045 \mu\text{m}$ rather than He I $2.059 \mu\text{m}$ (see below). This is also likely to be the case for the line at approximately the same wavelength seen in the 2010 eruption and tentatively identified as He I by Mason et al. (2012). Following the report of coronal line emission in the 2022 eruption (Banerjee et al. 2022), Rudy et al. (2022) reported re-examinations of their spectra of the 2010 outburst, and those of other observers (e.g., Banerjee et al. 2010; Mason et al. 2012; Maxwell et al. 2012). They noted the presence of coronal lines in the 2010 outburst as well, which either had not been identified, or had gone unnoticed.

2.3 The 2022 eruption

U Sco was reported to be in outburst on 2022 June 06.72 (MJD 59736.72; Moriyama 2022), which we take as the time

Table 1. Observing log.

2022 Date	MJD	Instrument	Resolution* ($\lambda/\Delta\lambda$)	λ range (μm)	Airmass		Day [†]	H (mag)	T_{BB} (K)
					U Sco	Standard			
June 12	59742.10	F2	200-1200	0.9–2.5	1.06	1.08	5.21	—	—
June 16	59746.13	F2	200-1200	0.9–2.5	1.03	1.04	9.41	11.64 ± 0.06	19000 ± 2000
June 17	59747.14	F2	200-1200	0.9–2.5	1.25	1.19	10.25	11.97 ± 0.05	16500 ± 1000
June 19	59747.14	F2	1700-3200	2.00–2.32	1.23	1.19	"		
	59749.11	F2	200-1200	0.9–2.5	1.03	1.03	12.22	12.37 ± 0.07	—
June 20	59749.11	F2	1700-3200	2.00–2.32	1.03	1.03	"		
	59750.47	SpeX	1200	0.7–2.55	1.65	1.55	13.59	—	—
June 30	59760.08	F2	200-1200	0.9–2.5	1.03	1.03	23.19	13.19 ± 0.08	20000 ± 1000
	59760.08	F2	1700-3200	2.00–2.32	1.03	1.03	"		
July 5	59765.10	F2	200-1200	0.9–2.5	1.19	1.19	28.21	13.86 ± 0.07	—
	59765.10	F2	1700-3200	2.00–2.32	1.27	1.32	"		
July 16	59776.27	GNIRS	1200	0.9–2.5	1.29	1.26	39.38	15.62 ± 0.14	—
July 22	59782.32	GNIRS	1200	0.9–2.5	1.34	1.32	45.43	15.48 ± 0.07	—

*See <http://www.gemini.edu/instrumentation/flamingos-2/components#Grisms> for how R for F2 varies across the spectral interval.

[†] $t = 0$ was at MJD 59736.72.

origin. The visual light curve from the AAVSO archive¹ is shown in Fig 1.

The 2022 eruption has been extensively observed at radio (Sokolovsky et al. 2022), optical (Siviero & Munari 2022; Woodward et al. 2022) and X-ray (Orio & Gendreau 2022; Page et al. 2022; Page & Osborne 2022) wavelengths. Preliminary descriptions of NIR observations were given by Banerjee et al. (2022) and Rudy et al. (2023). We present here the complete series of our NIR spectroscopic observations.

3 OBSERVATIONS

3.1 Gemini Observatory

Infrared spectra covering all, or portions, of the 0.9–2.5 μm wavelength interval were obtained at the Gemini South and North telescopes from 2022 June 12 to 2022 July 22 using the facility instruments FLAMINGOS-2 (F2; Eikenberry et al. 2004) and the Gemini Near-InfraRed Spectrometer (GNIRS; Elias et al. 2006). Observing details are provided in Table 1. Most of the spectra were obtained with the JH and HK grisms in F2, each of which provides resolving powers, R , ranging from 200 to 1400 (corresponding to 200–1500 km s^{-1}). Several higher resolution spectra of a large portion of the K band were obtained with F2’s R3k grism. GNIRS in its cross-dispersed mode and its $32 \ell \text{mm}^{-1}$ grating was employed for the final two epochs. Observing times varied from one minute during the early epochs when U Sco was bright, to 32 minutes for the final epoch when it had faded considerably.

A0 dwarfs served as telluric standards. They were observed at air masses closely matching those of U Sco, either immediately before, or immediately after, U Sco. Data reduction utilizing both IRAF (Tody 1986, 1993) and FIGARO (Currie et al. 2014) employed the standard procedures of spectrum extraction, spike removal, wavelength calibration (using spectra of argon arc lamps), removal of H I lines from the spectra of the standard star, cross-correlating

the spectra of U Sco and the telluric standard star, shifting the spectrum of the former to align it with the spectra of the standard star, and ratioing the former by the latter.

3.2 IRTF

NASA Infrared Telescope Facility (IRTF) observations were obtained with SpeX (Rayner et al. 2003) in short-crossed dispersed (SXD) mode with a $0'.5 \times 15''$ slit (spectral resolving power 1200, corresponding to $\simeq 250 \text{ km s}^{-1}$), in sub-arcsec seeing (FWHM [K] $\approx 0'.65$) under photometric conditions. The source was nodded between two positions along the slit. These data (comprising 478 s of total on-source integration time) were reduced and corrected for telluric absorption(s), flux calibrated, and order merged with the SpexTool pipeline (Cushing et al. 2004). The A0V standard star (for telluric correction) HD 148968 was observed at comparable air mass. The accuracy of flux calibration of the resultant spectra is $\simeq 10\%$.

Our time coverage is one of the longest over which an eruption of U Sco has been followed in the NIR. A difficulty with following this nova for longer periods is its very rapid fading, the time t_2 (t_3) to decline by 2 (3) magnitudes from maximum, being 1.2 (2.6) days (Schaefer 2010).

Where possible, aperture photometry was carried out on acquisition frames obtained in the H band to facilitate positioning of the object in the spectrograph slit. Calibration was achieved using multiple field stars with known H magnitudes from the 2MASS (Skrutskie et al. 2006) and UKIDSS (Dye et al. 2006) surveys. These H magnitudes are listed in Table 1, and included in Fig. 1. This figure also includes the H -band light curve from the 2010 eruption (Pagnotta et al. 2015, see that paper for details), on which our H band magnitudes are superposed. The 2022 H photometry agrees well with the 2010 H light curve, and there is excellent agreement between the shapes of the 2010 H and 2022 V light curves.

¹ <https://www.aavso.org/>

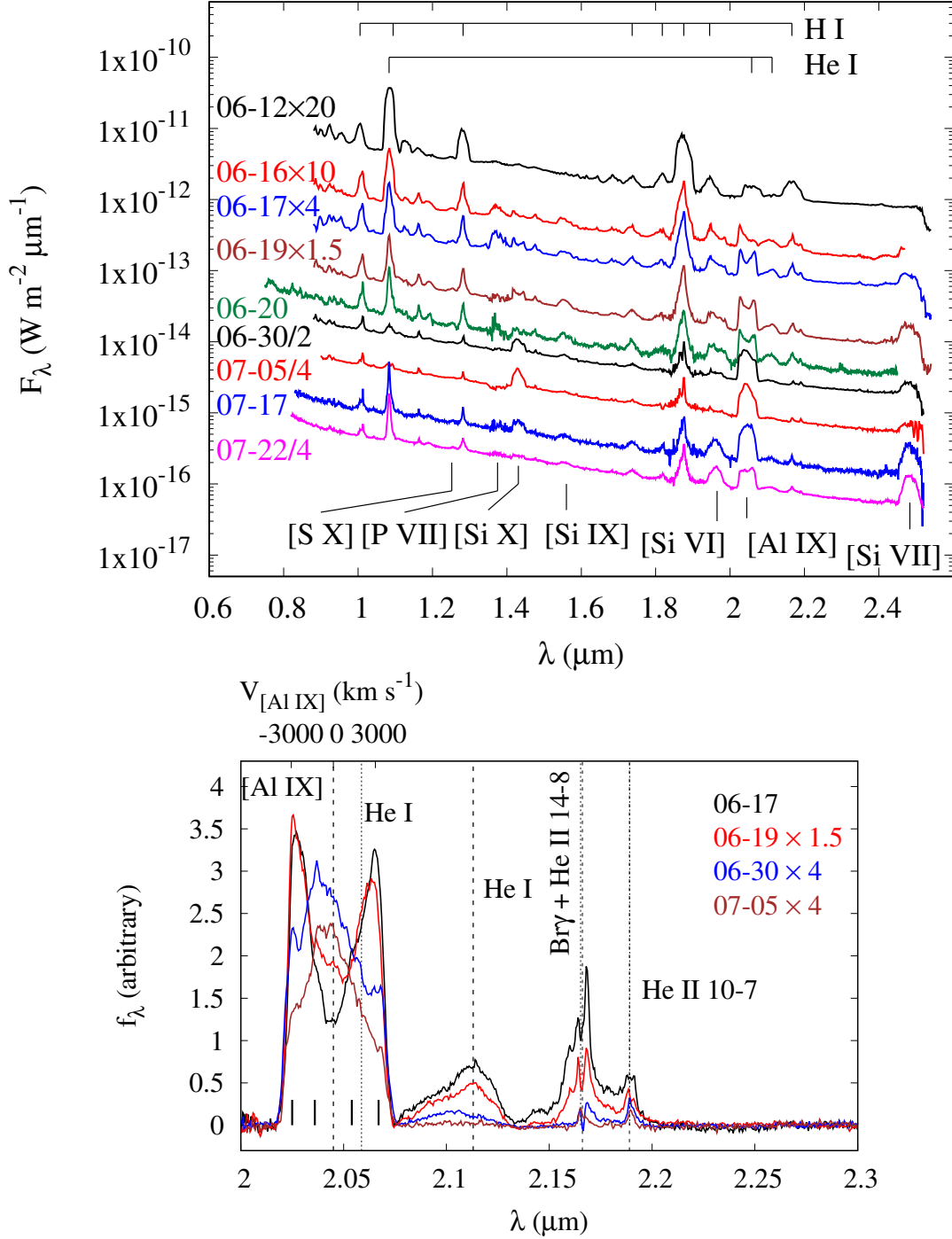


Figure 2. Top: sequence of lower resolution spectra. The 2022 spectra are labelled by date in the form MM-DD, and have been multiplied/divided by the factors indicated. Prominent H I, He I and coronal lines are identified. Bottom: R3k spectra, labelled by date in the form MM-DD, have been multiplied/divided by the factors indicated. Top radial velocity scale (in km s^{-1}) is for [Al IX] only. Black lines at bottom of panel indicate approximate wavelengths of the “core” and “horn” components. See text for details.

4 OVERVIEW OF THE SPECTRA

The lower resolution (≤ 1200) spectra are shown in Fig. 2 (top panel). H I recombination lines are prominent, but they are not useful for analysis, because they coincide with He II recombination lines. For example, six He II lines are close in wavelength to Br γ at $2.1661 \mu\text{m}$. The strongest of

these is the 10–7 transition at $2.1891 \mu\text{m}$, while He II 14–8 ($2.1652 \mu\text{m}$) almost exactly coincides with Br γ (see Fig. 2, bottom panel).

Low excitation lines are often seen in the IR spectra of novae in eruption (see compilation in Banerjee & Ashok 2012). However, other than the H I recombination lines,

there were no low excitation lines in the IR spectra of U Sco. O I 1.1287 μm was present up to day 10.25, but the upper level of this transition is pumped by Ly β fluorescence, thus pointing to a high excitation environment.

4.1 Coronal lines

A preliminary account of our data was given by Banerjee et al. (2022), who reported the first identification of coronal lines in an outburst of U Sco. Seven coronal lines: [Si IX] 1.252 μm , [P VII] 1.375 μm , [Si X] 1.431 μm , 1.560 μm , [Si VI] 1.965 μm , [Al IX] 2.045 μm and [Si VII] 2.483 μm were clearly present on day 9.41 (see Fig. 2). The last of these is at the extreme red end of the spectrum (where telluric correction is challenging), which limits its usefulness as a diagnostic. This is one of the earliest detection of coronal lines in any nova, classical or recurrent. Rudy et al. (2023) did not detect any of these coronal lines in a spectrum obtained only 20 hours earlier. We did not detect the [Ca VIII] line at 2.321 μm , which is often seen in the coronal phase of novae.

In the spectra of 16 June and later, we consider that the feature at $\sim 2.05 \mu\text{m}$ is mainly due to [Al IX] $\lambda = 2.045 \mu\text{m}$. He I $\lambda = 2.059 \mu\text{m}$ contributed partially on that date, but faded in subsequent spectra. This feature was present in both the low and high resolution data. In all cases the line profile is complex, and can (in common with several other lines) be divided into four components. The evolution of the [Al IX] line, as revealed by the high-resolution data, is shown in Fig 2. Its profile on June 17 and 19 has a characteristic “horned” structure, typical of jets² emitted orthogonal to the binary plane (Menzel & Payne 1933; Munari et al. 1999), together with two lower velocity components (the “core”) that likely arise in the binary plane. In time the horns decline in flux, while the core increases relative to the horns. There is no evidence that the velocities, as determined from the peak wavelengths of the lines, changed with time. The mean radial velocities, V_r , for the four components are $+2870 \pm 60 \text{ km s}^{-1}$, $+1000 \pm 130 \text{ km s}^{-1}$, $-770 \pm 130 \text{ km s}^{-1}$, and $-2660 \pm 80 \text{ km s}^{-1}$ (see Fig 3, left). Assuming that the horns do indeed arise in jets ejected perpendicular to the binary plane, the velocities, $V_0 = V_r / \cos i$, implied by these components, allowing for the binary inclination of $82^\circ.7$, are $+22600 \pm 1000 \text{ km s}^{-1}$, and $-20900 \pm 600 \text{ km s}^{-1}$ (see Fig. 3, left).

The above uncertainties are the standard errors in the mean radial velocities; including the uncertainty in the inclination ($\pm 2^\circ.9$) gives $+22600_{-6400}^{+14800} \text{ km s}^{-1}$, and $-20900_{-5900}^{+13700} \text{ km s}^{-1}$ respectively. However as U Sco is an eclipsing system, the constraint that the binary inclination $i > \cos^{-1}(R_*/a)$, where a is the binary separation ($6.5 R_\odot$; Thoroughgood et al. 2001) must be included, so that $i > 80^\circ$ for a K2IV secondary. This means that the lowest value allowed by these uncertainties is a physical lower limit. Remarkably, such high velocities are comparable to those measured in supernovae in the NIR (e.g., Hsiao et al. 2019).

A further, and compelling reason, to associate the horns with a fast polar flow, orthogonal to the binary orbital plane that contains a material overdensity (Drake & Orlando 2010), is that they are seen only in the coronal lines,

not in the H I lines (see Fig. 2). Assuming geometric dilution of the electron density $n_e \propto r^{-2}$, the coronal lines are expected to be first seen from regions that have dispersed the most rapidly, allowing the electron density to fall below the critical density for each transition. The kinematics of a bipolar flow, which is collimated by an equatorial overdensity, are such that matter along the polar direction always has the highest velocity, and thus declines most rapidly in density, allowing the emergence of coronal lines. At later times, emission in the coronal lines may be expected to be seen from other regions of the ejecta (e.g., matter in the equatorial region), as it is expanding at lower velocities and will thus take more time to drop below the critical density. The H I lines are likely to have been emitted from all regions of the ejecta. Horned profiles were also seen in the coronal lines, but not in the H and He lines, in the classical nova V5668 Sgr (see Figure 16 of Gehrz et al. 2018), who also argued that they arise in fast flowing polar material.

In our early spectra of the 2022 eruption, the [Si VI] 1.965 μm line (which was observed at low resolution only) is overwhelmed by Br δ at 1.9451 μm , but as the latter fades the [Si VI] line predominates. Its profile over the period June 17 to July 22 is shown in Fig. 4. The mean implied velocities of the horned components, allowing for the binary inclination, are $-24400 \pm 1200 \text{ km s}^{-1}$ and $12500 \pm 1300 \text{ km s}^{-1}$, where the uncertainties here are the standard errors of the means. Including the uncertainty in the binary inclination gives $-24400_{-6900}^{+16000} \text{ km s}^{-1}$ and $12500_{-3500}^{+8200} \text{ km s}^{-1}$ respectively (see Fig. 3, right).

The temperature of the coronal gas can be determined using the iterative method outlined in Woodward et al. (2021) and Evans et al. (2022). We assume $E(B - V) = 0.2 \pm 0.1$ (cf. Schaefer 2010), and use effective collision strengths Υ (i.e., the collision strength Ω averaged over a thermal electron energy distribution) from the Iron Project (Hummer et al. 1993; Lennon & Burke 1994; Galavis et al. 1997; Badnell et al. 2006) online database³, as well from the literature (Brage et al. 2000). The Υ values used are listed in Table 3.

In view of the complexities of the line profiles, one can not simply take ratios of total line fluxes, but must identify individual velocity components. The components most easily isolated are those that have the highest radial velocities, namely the “+2870 km s^{-1} ” and “-2660 km s^{-1} ” components (i.e., the horns/jets); we refer to these as the “red jet” and “blue jet” components respectively. We use the [Si VI] $\lambda = 1.965 \mu\text{m}$ and [Si X] 1.403 μm lines. The Si coronal line ([Si IX] $\lambda = 1.560 \mu\text{m}$) is problematic as it is superimposed on higher order members of the hydrogen Brackett series.

The coronal temperatures T_{cor} for these components are listed in Table 2. There is no evidence for any temporal change in T_{cor} for either component, the mean values being (T_{cor} in K) $\log T_{\text{cor}} = 5.88 \pm 0.04$ for the blue jet component, and $\log T_{\text{cor}} = 5.82 \pm 0.04$ for the red jet component; the overall mean is $\log T_{\text{cor}} = 5.85 \pm 0.03$ ($T_{\text{cor}} = 7.1[\pm 0.5] \times 10^5 \text{ K}$, $kT = 61.3 \text{ eV}$), which we use henceforth.

The critical electron densities (above which the upper levels are mainly collisionally rather than radiatively de-excited), are given in Table 3. They have been calculated at

² By “jets” here we mean highly collimated outflows.

³ <http://cdsweb.u-strasbg.fr/tipbase/home.html>

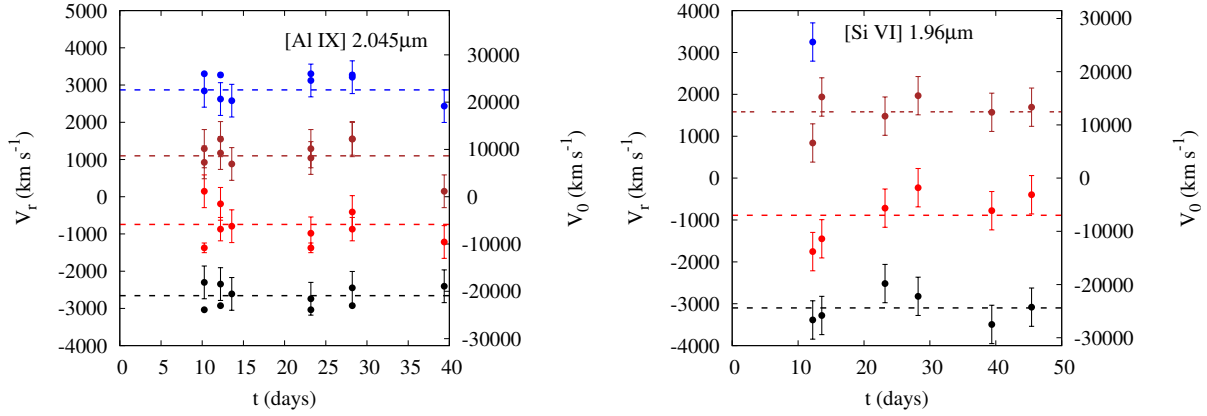


Figure 3. Left: velocities as determined from the [Al IX] line; left axis, radial velocity V_r , right axis, velocity V_0 after allowing for binary inclination. Red points and lines, core components; blue/black lines and points, horn components. Right: velocities as determined from the [Si VI] line; left axis, radial velocity, right axis, velocity after allowing for binary inclination. The blue point is the fourth component, seen at day 9.41 only. Red points and lines, core components; black line and points, horn components. In both panels dashed lines are mean radial velocities.

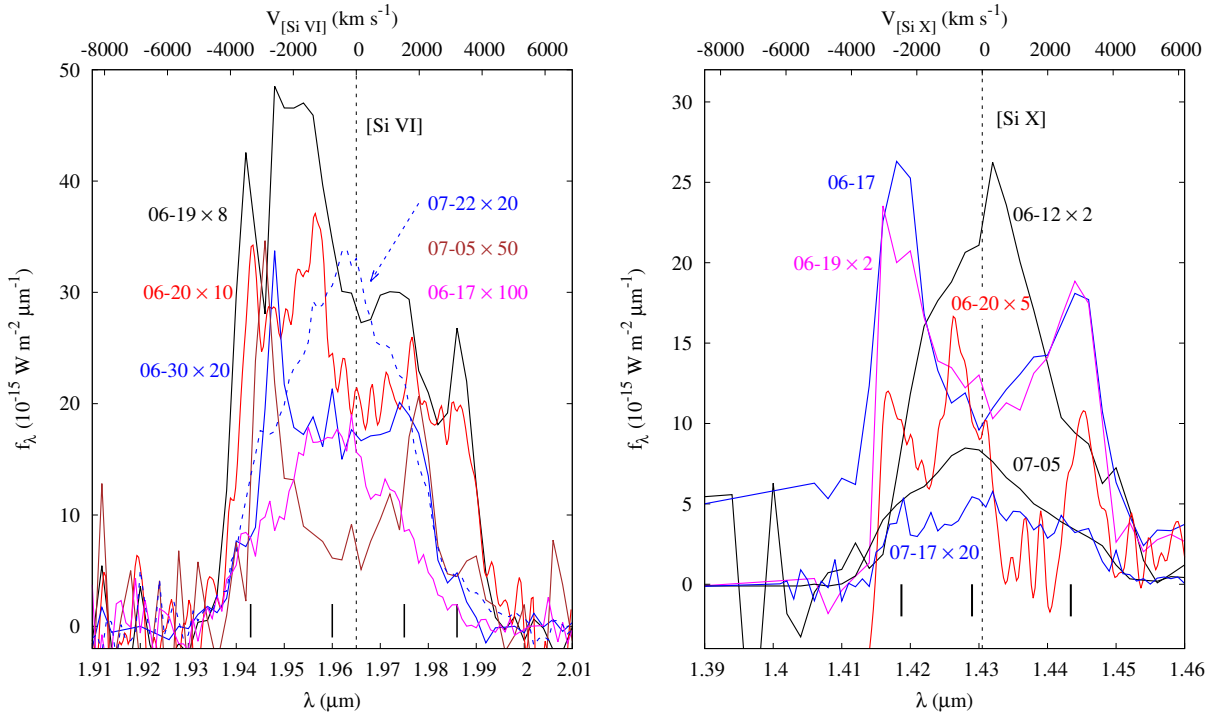


Figure 4. Left: Evolution of the [Si VI] 1.965 μm profile as revealed by the low resolution spectroscopy; dates are given in the form MM-DD, and spectra have been multiplied by the values indicated. Right, as left, for selection of [Si X] 1.431 μm profiles. In each case the top scale gives the radial velocity, and the black lines at bottom of panels indicate approximate wavelengths of the “core” and “horn” components.

log $T_{\text{cor}} = 5.85$, except for [S IX] and [Si VII], for which 10^5 K is the highest value available in the Iron Project database.

4.2 The He I lines

On June 12 (day 5.21), the He I 1.083 μm line was broad, with at least four components. Thereafter, it consisted of a strong core, with wings to the blue and red (see Fig. 5, top panel). In each spectrum there is almost certainly a contribution from Pa γ 1.094 μm , which is superimposed on the

contribution from any red wing the He I line may have. For plasma temperatures up to 3×10^4 K, the Pa γ flux is expected to be ~ 0.6 that of Pa β for a wide range of electron densities if “Case B” applies. Thus, for example, on June 16 Pa γ would have had a peak flux above the adjacent continuum of $\sim 9 \times 10^{-14}$ $\text{W m}^{-2} \mu\text{m}^{-1}$, comparable with $\sim 7 \times 10^{-14}$ $\text{W m}^{-2} \mu\text{m}^{-1}$ for the peak of the red wing of the observed feature, and much less than the 4.1×10^{-13} $\text{W m}^{-2} \mu\text{m}^{-1}$ for the peak of He I itself. Therefore, in our analysis below, we consider the blue wing only.

Table 2. Coronal gas temperatures for the “jets”, determined using Si lines as described in text.

Date	Day	log T (K)	
		Blue jet	Red jet
June 16	9.41	6.03	6.01
June 17	10.25	5.90	5.80
June 19	12.22	5.82	5.76
June 30	23.19	6.02	5.90
July 5	28.21	5.77	5.70
July 16	39.38	5.75	5.76
July 22	45.43	5.90	5.83

Table 3. Critical densities at 7.1×10^5 K for coronal lines. IP is the ionisation potential of the lower ionisation state. Υ is the effective collision strength at 7.1×10^5 K unless otherwise noted. See text for details, and for definition of T_* .

Line	λ (μm)	IP (eV)	kT_* (eV)	Υ	$n_{\text{crit}}(\text{cm}^{-3})$
[Si IX]	1.252	329	137	0.907*	6.30×10^9
[P VII]	1.375	220	93	0.315	4.30×10^9
[Si X]	1.431	351	146	0.415	1.01×10^9
[Si IX]	1.560	304	127	0.275*	1.02×10^9
[Si VI]	1.965	167	70	0.404	2.32×10^9
[Al IX]	2.045	285	119	0.720	2.94×10^8
[Si VII]	2.483	205	86	0.695*	1.04×10^9

*At 10^5 K.

The central wavelengths of the core and blue wings have been converted to radial velocities, as shown in Fig. 5. There is no evidence that the radial velocity of the material responsible for the core component changes with time. The implied radial velocity is essentially zero (mean value = $95 \pm 120 \text{ km s}^{-1}$). The mean FWHM of the core emission is $750 \pm 100 \text{ km s}^{-1}$. The wavelength of peak flux of the core is close to zero; thus we conclude that this component arises in material (e.g., a torus) ejected in the orbital plane, almost perpendicular to the plane of the sky.

On the other hand there is some evidence that the material emitting the blue wing decelerated as

$$V_r(\text{km s}^{-1}) = -3260[\pm 280] + 49[\pm 11] t$$

where t is in days. The implied deceleration is considerably less than that implied by the narrowing of H α during the 2010 eruption (Munari et al. 1999), but is of the same order as the deceleration implied by the narrowing of Pa β in the 2019 eruption of V3890 Sgr (Evans et al. 2022). The initial radial velocity of the blue wing ($\simeq -3000 \text{ km s}^{-1}$) is close to that of the [Al IX] line ($\simeq -2700 \text{ km s}^{-1}$; see Fig. 3, left panel), suggesting that the blue wing of the He I 1.0833 μm line arises in the same jets as the material responsible for [Al IX]. If this is the case the deprojected velocities approach 25000 km s^{-1} .

We attribute the feature at $2.116 \mu\text{m}$ to a blend of He I $1^1\text{S}^1\text{P}^o \lambda = 2.1138 \mu\text{m}$ and $3^1\text{P}^o\text{-}3^1\text{S} \lambda = 2.1120 \mu\text{m}$ (see Fig. 2). This feature is commonly seen in erupting novae (Raj 2015, and references therein), and was present in the 2019 eruption of the RN V3890 Sgr (Evans et al. 2022). In the high resolution spectra, the feature is asymmetric at the earliest epoch, with a weak blue wing superposed on a

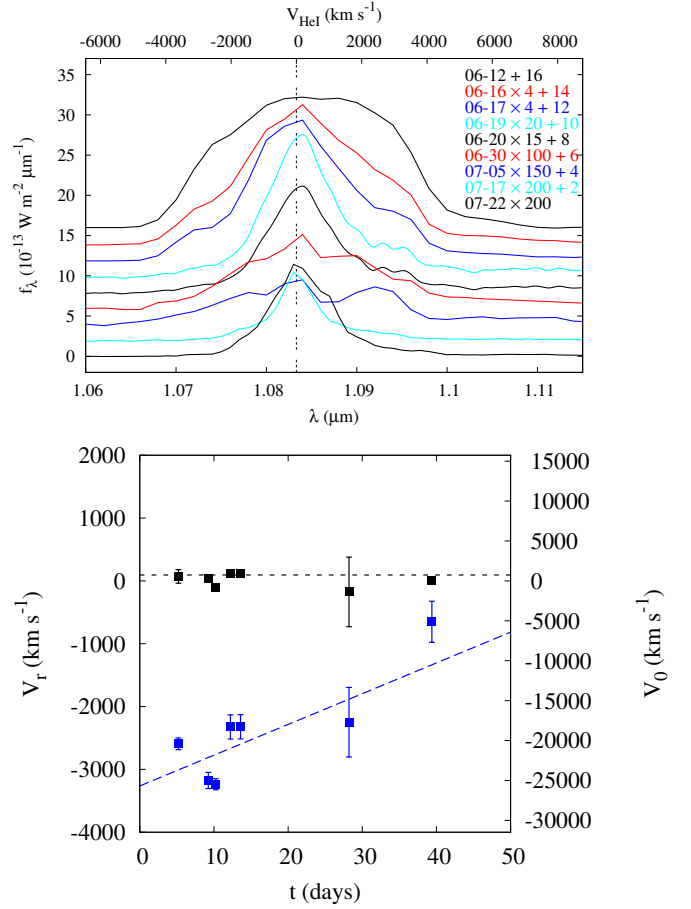


Figure 5. Top: evolution of the He I 1.083 μm profile as revealed by low resolution spectroscopy. Spectra have been multiplied and displaced by the factors indicated. Dates (2022) are given in the form MM-DD. Bottom: velocities of the core (filled black squares) and blue (filled blue squares) wing components of He I 1.083 μm . The left-hand axis gives the radial velocity V_r ; the right-hand axis gives the space velocity V_0 (after allowing for binary inclination) giving rise to the blue wing. Black dotted line is the mean velocity as determined from the peak of the He I 1.0833 μm core; blue dotted line is a linear fit to the He I 1.0833 μm wing.

stronger core. Although the line weakened considerably after \sim day 12, making the properties of the two components difficult to measure, fitting two gaussians to it reveals a picture that is broadly similar to the He I 1.0833 μm line (see Fig. 5), supporting the view that it is due to He I (rather than [Ca IX]; see Evans et al. 2022). However, there is also a distinct possibility that this feature has a contribution from an unidentified coronal line at $\sim 2.1 \mu\text{m}$, seen earlier in several classical novae, for example V1974 Cyg (Wagner & Depoy 1996), V959 Mon (Banerjee et al. 2012), and V5668 Sgr (Gehrz et al. 2018).

The presence of a He I line in the coronal gas at temperature 7.1×10^5 K is very surprising. At this temperature, essentially all the helium is doubly-ionised (see Arnaud & Rothenflug 1985). This suggests that there is a region of the circumstellar environment in which the temperature is considerably lower. The data in Arnaud & Rothenflug (1985) suggest that, below 2.2×10^4 K, helium is predominantly neutral, whereas between 4×10^4 K and $\sim 6.3 \times 10^4$ K it

Table 4. Swift photometry. Data are in magnitudes.

Swift filter: Effective λ (Å) = Day*	<i>v</i> 5410	<i>b</i> 4321	<i>u</i> 3442	<i>uvw1</i> 2486	<i>uvm2</i> 2221	<i>uvw2</i> 1991
4.53	11.46 ± 0.03	—	—	—	11.02 ± 0.03	—
9.09	13.04 ± 0.03	12.81 ± 0.03	—	11.84 ± 0.02	12.07 ± 0.03	11.75 ± 0.02
9.25	—	—	—	—	—	12.09 ± 0.03
10.09	13.17 ± 0.03	13.03 ± 0.03	12.04 ± 0.03	12.06 ± 0.02	12.31 ± 0.03	12.04 ± 0.02
10.22	—	—	—	11.98 ± 0.02	—	12.03 ± 0.03
12.08	13.73 ± 0.03	13.68 ± 0.03	12.65 ± 0.03	12.53 ± 0.02	12.81 ± 0.03	12.57 ± 0.02
12.30	—	—	—	—	—	12.98 ± 0.03
13.41	13.94 ± 0.04	13.92 ± 0.03	12.89 ± 0.03	12.81 ± 0.03	13.03 ± 0.03	12.86 ± 0.02
13.62	—	—	—	—	12.92 ± 0.03	12.67 ± 0.03
23.22	14.44 ± 0.04	14.63 ± 0.03	13.50 ± 0.03	13.40 ± 0.03	13.58 ± 0.03	13.43 ± 0.02
27.47	14.58 ± 0.04	14.80 ± 0.03	13.61 ± 0.03	13.57 ± 0.03	13.71 ± 0.03	13.59 ± 0.03
28.67	—	—	—	—	13.96 ± 0.04	13.85 ± 0.04
38.80	16.25 ± 0.10	16.21 ± 0.05	15.23 ± 0.05	15.20 ± 0.05	15.40 ± 0.06	15.25 ± 0.04
42.72	16.86 ± 0.14	17.15 ± 0.09	16.26 ± 0.07	16.14 ± 0.07	16.62 ± 0.09	16.19 ± 0.06
45.83	—	—	16.24 ± 0.11	16.39 ± 0.08	—	—

*Day numbers, with $t = 0$ at MJD 59736.72, are means of individual values.

is primarily in the form of He II. He III predominates above $\sim 8 \times 10^4$ K. We conclude that, in addition to the hot (7.1×10^5 K) “coronal” region, there must exist a cooler ($\lesssim 2 \times 10^4$ K) region where the helium is neutral. We suggest that this material resides in the torus containing the 750 km s^{-1} gas, postulated above.

There may be some supporting evidence for the existence of the orbital plane torus in the Swift X-ray data, which imply a hydrogen absorbing column of $N_{\text{H}} \simeq 3 \times 10^{21} \text{ cm}^{-2}$ along the line of sight to U Sco. Using the conversion given by Liszt (2014) for the interstellar medium,

$$N(\text{H I})/E(B - V) = 8.3 \times 10^{21} \text{ cm}^{-2} \text{ mag}^{-1},$$

together with the assumed $E(B - V) = 0.2$, suggests that only $\sim 1.7 \times 10^{21} \text{ cm}^{-2}$ of this is interstellar. The difference between these values, $\sim 1.3 \times 10^{21} \text{ cm}^{-2}$, presumably is due to H I in the circumstellar environment. Even allowing for the uncertainty in $E(B - V)$, the difference is at least $\sim 5 \times 10^{20} \text{ cm}^{-2}$.

To estimate the H I column density in the circumstellar gas, we assume wind density $\propto r^{-2}$, ejected over a period δt ($\simeq 20$ days; Hachisu et al. 2000). The column density at time t is

$$N \simeq \frac{\dot{M}}{4\pi\bar{m}V^2} \frac{\delta t}{t(t - \delta t)},$$

(cf., Evans et al. 2022) where \dot{M} is the mass ejection rate in the eruption and \bar{m} is the mean atomic mass. For a mass-loss rate $\sim 10^{-7} M_{\odot} \text{ yr}^{-1}$ (Hachisu et al. 2000), $V = 750 \text{ km s}^{-1}$ for the core component (see above), and $\bar{m} \simeq 1$,

$$N \sim 1.2 \times 10^{22} \frac{\delta t}{t(t - \delta t)} \text{ cm}^{-2},$$

where both t and δt are in days, so that $N \sim 8 \times 10^{20} \text{ cm}^{-2}$ after ~ 30 days. Given the crudeness of the analysis, and the uncertainty in converting $E(B - V)$ to N_{H} , this is surprisingly close to the estimated circumstellar contribution to N_{H} .

4.3 The IR continuum

We have obtained *BVI* photometry of U Sco from the AAVSO database. We also have UV/Optical Telescope (UVOT) photometry from the Neil Gehrels Swift Observatory (Gehrels et al. 2004), in the *v* (5468Å), *b* (4392Å), *u* (3465Å), *uvw1* (2600Å), *uvm2* (2246Å), *uvw2* (1928Å) filters; the Swift photometry is given in Table 4.

At the shortest ($\lesssim 1 \mu\text{m}$) wavelengths, the data are reasonably fitted by a black body function. However, for a more satisfactory fit we require photometry at the shortest wavelength (*uvw2*), together with complementary photometry at longer wavelengths. We select UVOT and AAVSO data within < 88 min ($< 10\%$ of the orbital period) of the IR spectroscopy. The datasets that satisfy these criteria are for June 16, June 17 and June 30 (see Fig. 6). We have fitted black body curves to the UVOT/*BVR* data; the black body temperatures, T_{BB} , are 19000 ± 2000 K (June 16), 16500 ± 1000 K (June 17), 20000 ± 1000 K (June 30). We have also fitted black body curves to Swift data that do not coincide closely with the IR data. Fig. 7 shows the time-dependence of T_{BB} , its bolometric flux and luminosity, and the angular diameter and linear size of the emitter. A distance of 10 kpc has been assumed. The temperature of the black body remained constant (~ 20000 K) over the 40 days of our IR observations, but its flux/luminosity, and therefore its dimensions, declined significantly.

Evans et al. (2001) suggested that the black body might be the WD itself, but this can not be the case, as the nova is in the “Super Soft” X-ray phase⁴, and therefore much hotter, at this time (see below). Neither can it be the accretion disc, the bolometric luminosity of which in U Sco is $\sim 535 L_{\odot}$ for an accretion rate of $2.5 \times 10^{-7} M_{\odot} \text{ yr}^{-1}$ (Hachisu et al. 2000) and a $1.37 M_{\odot}$ WD of radius $0.01 R_{\odot}$. This luminosity is of the same order as that of the black body; moreover, the dimensions are comparable with the binary separation. However, as the disc in U Sco is seen almost edge-on, the ob-

⁴ See e.g. Page, Beardmore & Osborne (2020) for an explanation.

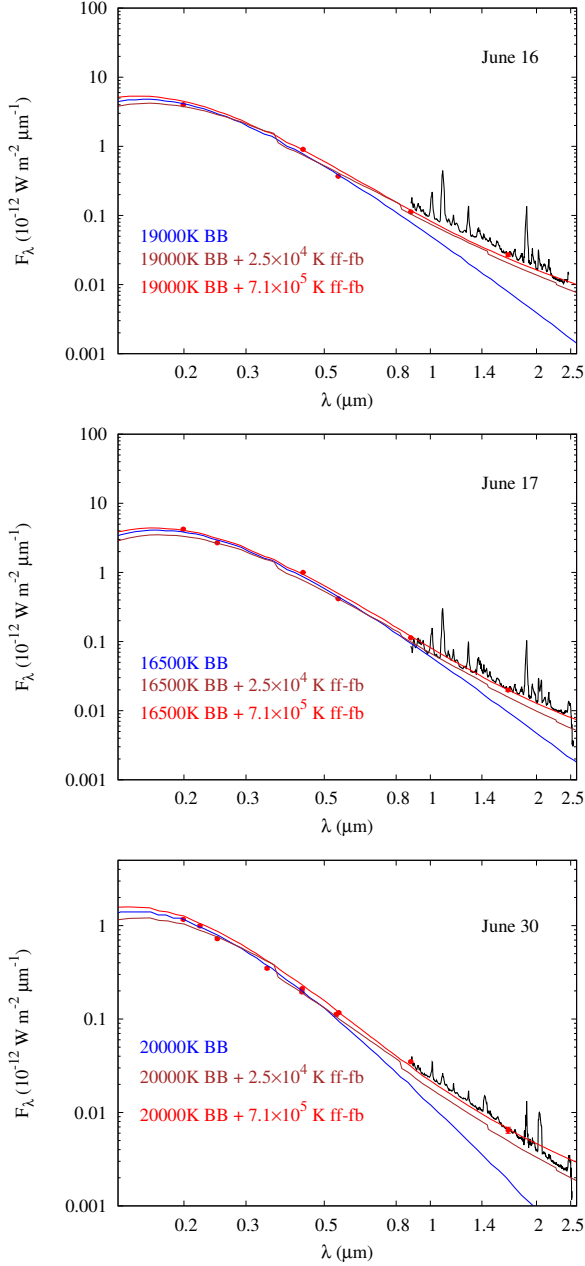


Figure 6. Top: UV-optical-NIR SED of *U Sco* on June 16. Data dereddened by $E(B-V) = 0.2$. Red points: Swift UVOT photometry and *H* band photometry obtained as described in Section 3. Blue curve is black body fit to UVOT data. Red curve is black body + free-free/free-bound emission at $7.1 \times 10^5 \text{ K}$; brown curve is black body + free-free/free-bound emission at $2.5 \times 10^4 \text{ K}$. Middle: as top, but for June 17. Bottom: as top, but for June 30. In all cases, helium is entirely neutral for the $2.5 \times 10^4 \text{ K}$ case, and completely ionised for the $7.1 \times 10^5 \text{ K}$ See text for details.

served luminosity of the disc is less than the accretion luminosity. Using the formalism of Paczyński & Schwarzenberg-Czerny (1980) for a standard limb-darkened disc (i.e., one that has not been subject to a nova eruption), we find that the bolometric luminosity of a nearly-edge-on disc is fainter than that of one seen face-on by a factor $\sim 1.1 \times 10^{-3}$. In any case it is very likely that the accretion disc is destroyed early in the eruption (Drake & Orlando 2010).

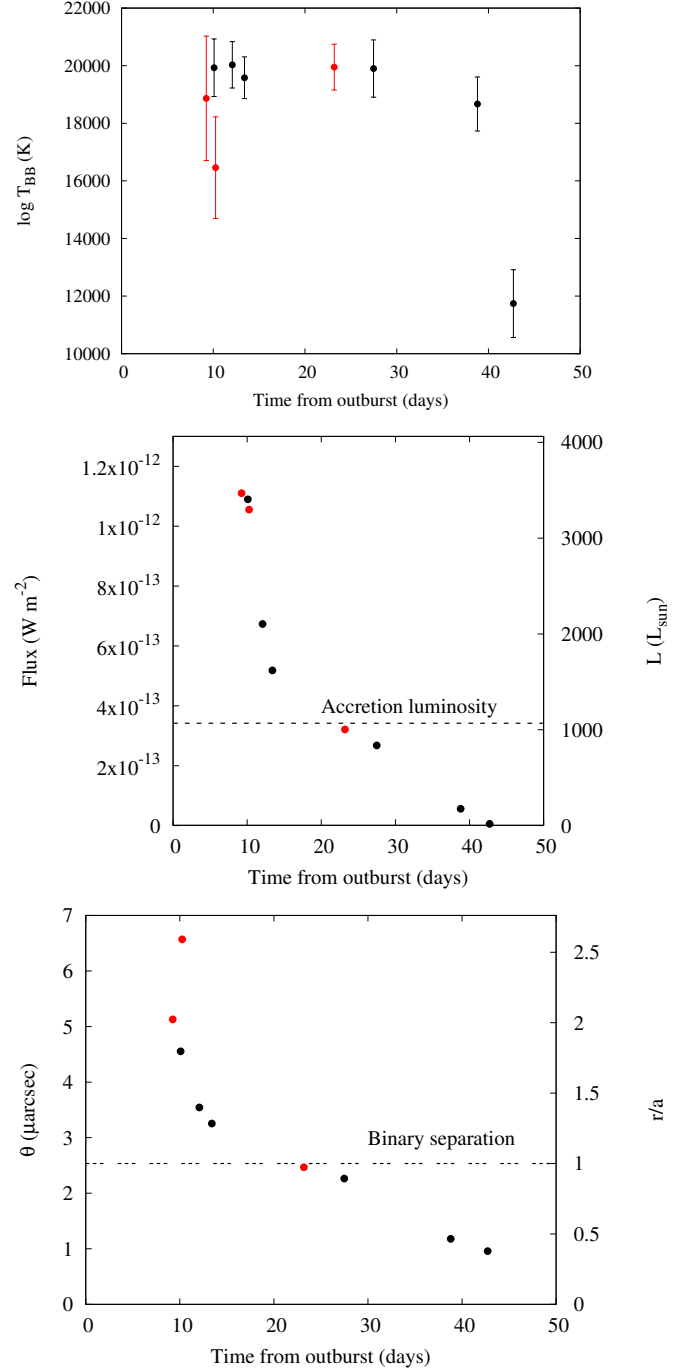


Figure 7. Top: time-dependence of T_{BB} . Middle: time-dependence of black body flux (left axis), and luminosity, assuming 10 kpc distance (right axis). Bottom: time-dependence of black body angular diameter (in μarcsec , left axis) and diameter (in units of binary separation, right axis) of black body. Distance assumed is 10 kpc; binary separation assumed is $6.5 R_{\odot}$ (Thoroughgood et al. 2001). Black points, black body fits to Swift data; red points, black body fits to Swift data within 88 min of IR observations.

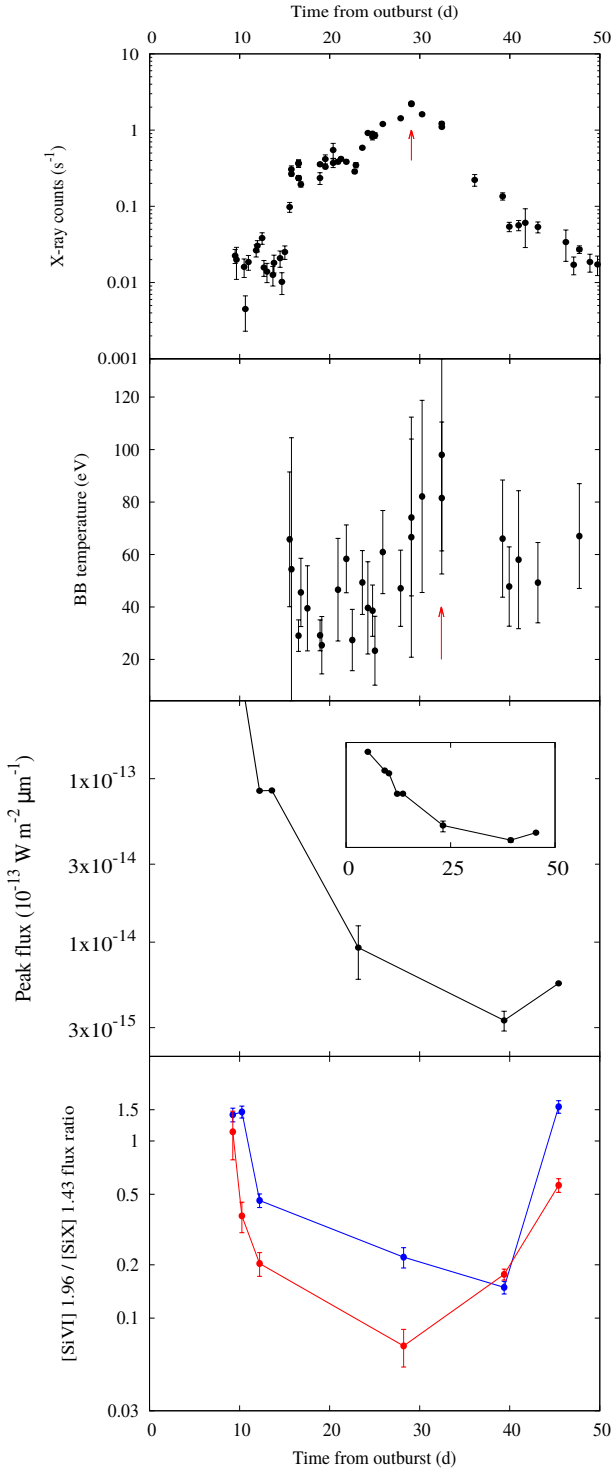


Figure 8. Top: Swift X-ray counts; arrow indicates maximum count rate. Upper middle: Black body temperature of the Swift source; arrow indicates maximum temperature. Lower middle: evolution of the peak flux of the He I 1.0833 μm line. Inset shows entire decline over the period of our observations. Bottom: evolution of the [Si VI] 1.96 μm /[Si X] 1.43 μm flux ratio. Red points, fluxes of receding jets, blue points those of approaching jets (see Section 4.1).

Might the black body be the secondary star? The K2IV secondary has radius $2.1 R_{\odot}$ (Thoroughgood et al. 2001); assuming effective temperature $T_{\text{eff}} \simeq 4600$ K, typical of field K2 stars (Zombeck 1990), the bolometric luminosity $L_{\text{bol}} \sim 1.8 L_{\odot}$. Thus the black body can not be the pristine secondary. However, in the absence of the accretion disc (which is destroyed in the eruption), the secondary must be irradiated by the hot WD. We estimate this effect using the formalism of Kovetz, Prrialnik & Shara (1988). For a WD temperature given by $kT_{\text{WD}} \simeq 60$ eV (see Fig. 8 below), the temperature of the irradiated secondary is $T_{\text{irr}} \simeq 19400$ K, with a corresponding luminosity $\sim 545 L_{\odot}$. The observed black body temperature is therefore close to that expected for an irradiated secondary, while the luminosity is of the same order. Given the crude nature of our estimates, the irradiated secondary seems the least unlikely explanation.

Notwithstanding the nature of the black body seen in the NIR, the comparison of the Swift and NIR data shows that there is clear excess radiation in the NIR, as noted by Evans et al. (2001). We interpret this as free-free/free-bound emission. We have fitted the excess with a free-free/free-bound continuum, using the observed H β flux of $\simeq 1.31 \times 10^{-11}$ ergs s⁻¹ cm⁻² (Woodward et al. 2022), which provides an estimate of the continuum level. For simplicity, we assume that the electrons arise from H and He only, and gas temperatures of 7.1×10^5 K (corresponding to the coronal gas, in which the He is completely ionised) and 2.5×10^4 K (in which the He is neutral). The calculation of the free-free/free-bound emission is done separately for the two temperatures. These are included in Fig. 6. There is essentially no difference between the hotter and the cooler free-free/free-bound emission for June 16 and 30. However the hotter continuum overshoots the UVOT data for June 17; the continuum coming from the cooler gas is in close agreement. We tentatively suggest that the free-free continuum arises in the cooler region from which the He I lines originate (see Section 4.2).

4.4 Coronal line excitation

The spectra in Fig. 2 reveal the remarkable fall and rise of the He I 1.0833 μm line. The dependence of its peak flux (continuum-subtracted) is shown in the lower middle panel of Fig. 8 (estimating the total line flux is complicated due to variations in the line width). The variation in the He line are replicated in the evolution of the [Si VI] emission line at 1.965 μm , which is seemingly absent after day 23.19, only to reappear on day 39.38. This is demonstrated by the flux ratio [Si VI] 1.96 μm /[Si X] 1.43 μm , using the fluxes used to determine the coronal gas temperatures given in Table 2. This ratio, which gives a measure of the relative excitation of the gas, also reaches a minimum at ~ 30 days. These relationships are also shown in Fig. 8, in which the upper two panels are the Swift X-ray counts and black body temperature of the X-ray source. Given the relatively low cadence of our IR observations, the data are consistent with the He I line flux, and the [Si VI]/[Si IX] flux ratio, both reaching minima between days 29.21 and 39.38.

The X-ray counts reach a maximum on day 29.1. The black body temperature (T_{WD}); note the distinction between this black body temperature and that discussed in Section 4.3) of the Swift source, which we identify with that

of the WD, peaks at $kT_{\text{WD}} \simeq 98$ eV ($T_{\text{WD}} \simeq 1.1 \times 10^6$ K), on day 32.4. The X-ray counts and T_{WD} peak at around the same time. Thus there seems to be a correlation between the time of the minima in the fluxes of the He I and [Si VI] lines, and of the peaks in the X-ray counts and T_{WD} .

The behaviour of the flux ratio of the two Si lines (Fig. 8; [Si VI], IP = 167 eV; [Si X]), IP = 351 eV) clearly demonstrates that the degree of ionisation peaked around day ~ 30 , despite the fact that the black body temperature of the Swift X-ray source rarely exceeds $kT_{\text{WD}} \sim 60$ eV.

Included in Table 3 are the ionisation potentials of the lower ionisation stages (e.g., the ionisation potential of Si V for [Si VI]), and the temperatures T_* at which half the photons emitted by the corresponding black body can ionise the lower ion (see Woodward et al. 2022). The dependence of T_{WD} on time shows no value on day 5.21 (see Fig. 8), when the X-ray counts were too low to provide a solution. However, at the earliest times, $kT_{\text{WD}} \sim 50$ eV, which seems too low to photoionise and produce any of the high-ionisation coronal lines seen (e.g., [Al IX], [Si VII], [Si X]).

We tentatively conclude that shock ionisation and excitation must be operating throughout the eruption, but that photoionisation also contributes, possibly significantly, at around the soft X-ray peak when the WD temperature was at its maximum.

In the absence of a secondary wind (as is present in the case of RNe with giant secondaries), presumably internal shocks arise in collisions between parcels of ejecta moving at different velocities. However a definitive conclusion must await a robust analysis of the dynamics of the eruption.

5 CONCLUSION

We have presented near-infrared spectra of the RN U Sco, covering the period 5.2 to 45.4 days after its 2022 eruption. This is the most intensive infrared observations of this object. We find that

- (i) coronal lines were present at 9.41 days after the outburst, one of the earliest appearances of coronal lines in a nova, classical or recurrent;
- (ii) the temperature of the coronal gas was 7.1×10^5 K, and there is evidence for the simultaneous presence of much cooler ($\lesssim 2 \times 10^4$ K) gas;
- (iii) there is evidence in the IR data for a 20000 K black body, which we tentatively identify with the secondary, irradiated by the hot white dwarf;
- (iv) the ejecta are distributed partly in polar “jets” in which the coronal lines largely arise, and an equatorial “torus” in the binary plane, from which line emission from the cooler gas originates;
- (v) for orbital inclination $82^\circ.7$, jet ejection velocities as high as 2×10^4 km s $^{-1}$ are implied. These are comparable with velocities seen in some supernovae.

These properties mark U Sco as a truly remarkable system.

ACKNOWLEDGEMENTS

We thank the referee for their careful and thorough review of the paper.

The Gemini observations were made possible by awards of Director’s Discretionary Time for programmes GS-2022A-DD-105 and GN-2022A-DD-105.

The international Gemini Observatory is a program of NSF’s NOIRLab, which is managed by the Association of Universities for Research in Astronomy (AURA) under a cooperative agreement with the National Science Foundation, on behalf of the Gemini Observatory partnership: the National Science Foundation (United States), National Research Council (Canada), Agencia Nacional de Investigación y Desarrollo (Chile), Ministerio de Ciencia, Tecnología e Innovación (Argentina), Ministério da Ciência, Tecnologia, Inovações e Comunicações (Brazil), and Korea Astronomy and Space Science Institute (Republic of Korea).

The IRTF observations were conducted under programme 2022A003. The Infrared Telescope Facility is operated by the University of Hawaii under contract 80HGTR19D0030 with the National Aeronautics and Space Administration.

CEW acknowledges partial support from NASA grant 80NSSC19K0868. DPKB is supported by a CSIR Emeritus Scientist grant-in-aid and is being hosted by the Physical Research Laboratory, Ahmedabad. RDG was supported by the United States Airforce. KLP acknowledges funding from the UK Space Agency. SS acknowledges partial support from an ASU Regents’ Professorship.

We acknowledge with thanks the variable star observations from the AAVSO International Database contributed by observers worldwide and used in this research.

DATA AVAILABILITY

The raw infrared data in this paper are available from the Gemini Observatory Archive, <https://archive.gemini.edu/>, and from the IRTF archive, http://irtfweb.ifa.hawaii.edu/research/irtf_data_archive.php. The Swift data are available from https://www.swift.ac.uk/swift_live/ and <https://heasarc.gsfc.nasa.gov/cgi-bin/W3Browse/w3browse.pl>

REFERENCES

- Anupama G. C., 2008, in RS Ophiuchi (2006) and the Recurrent Nova Phenomenon, Astronomical Society of the Pacific Conference Series, eds A. Evans, M. F. Bode, T. J. O’Brien, M. J. Darnley, vol. 401, p. 31, San Francisco
- Anupama G. C., et al., 2013, *A&A*, 559, A121
- Arnaud M., Rothenflug R., 1985, *A&AS*, 60, 425
- Astropy Collaboration, Price-Whelan, A. M., Sipőcz, B. M., et al., 2018, *AJ*, 156, 123
- Badnell N. R., Bautista M. A., Berrington K. A., et al. 2006, in IAU Symposium 234, Planetary Nebulae in our Galaxy and Beyond, ed. M. J. Barlow, R. H. Méndez (Cambridge: Cambridge University Press), 211
- Banerjee D. P. K., et al., 2010, *MNRAS*, 408, L71
- Banerjee D. P. K., Ashok N. M., 2012, *BASI*, 40, 243
- Banerjee D. P. K., Ashok N. M., Venkataraman V., 2012, *ATel*, 4542
- Banerjee D. P. K., et al., 2022, *ATel* 15451

- Barlow M. J., et al., 1981, MNRAS, 195, 61
- Brage T., Judge P. G., Jönsson P., Edwards D. P., 2000, ApJ, 540, 1114
- Currie M. J., Berry D. S., Jenness T., Gibb A. G., Bell G. S., Draper P. W., 2014, in Manset N., Forshay P., eds, *Astronomical Society of the Pacific Conference Series Vol. 485, Astronomical Data Analysis Software and Systems XXIII*. Astron. Soc. Pac., San Francisco, p. 391
- Cushing M. C., Vacca W. D., Rayner J. T., 2004, PASP, 116, 362
- Darnley M. J., 2021, in *The Golden Age of Cataclysmic Variables and Related Objects V. Proceedings of Science, 2-7 September 2019, Palermo, Italy*, p. 44
- Drake J. J., Orlando S., 2010, ApJ Letters, 720, L195
- Dye S., et al., 2006, MNRAS, 372, 1227
- Eikenberry S. S., et al., 2004, Proc. SPIE, 5492, 1196
- Elias J. H., Rodgers B., Joyce R., Lazo M., Doppmann G., Winge C., Rodriguez-Ardila A., 2006, Proc. SPIE, 6269, 14
- Evans A., et al., 2001, A&A, 378, 132
- Evans A., et al., 2022, MNRAS, 517, 6077
- Galavis M. E., Mendoza C., Zeppen C. J., 1997, A&AS, 123, 159
- Gehrels N., et al., 2004, ApJ, 611, 1005
- Gehrz R. D., et al., 2018, ApJ, 858, 78
- Hachisu I., Kato M., Kato T., Matsumoto K., 2000, ApJ, 528, L97
- Hsiao E. Y., et al., 2019, PASP, 131, 014002
- Hummer D. G., Berrington K. A., Eissner W., et al., 1993, A&A, 279, 298
- Iijima T., 2002, A&A, 387, 1013
- Kahabka P., Hartmann H. W., Parmar A. N., Negueruela I., 1999, A&A, 347, L43
- Kovetz A., Prialnik D., Shara M. M., 1988, ApJ, 325, 828
- Lennon D. J., Burke V. M., 1994, A&AS, 103, 273
- Liszt H., 2014, ApJ, 783, 17
- Mason E., 2013, A&A, 556, C2
- Mason E., Ederoclite A., Williams R. E., Della Valle M., Setiawan J., 2012, A&A, 544, A149
- Maxwell M. P., et al., 2012, MNRAS, 419, 1465
- Maxwell M. P., et al., 2015, MNRAS, 448, 3414
- Menzel D. H., Payne C. H., 1933, PNAS, 19, 641
- Moriyama M., 2022, vsnet-alert 26798
- Munari U., et al., 1999, A&A, 347, L39
- Orio M., Gendreau K., 2022, ATel 15436
- Paczynski B., Schwarzenberg-Czerny A., 1980, Acta Astron., 30, 127
- Page K. L., Beardmore, A. P., Osborne J. P., 2020, Adv. Sp. Res., 66, 1169
- Page K. L., et al., 2022, ATel 15438
- Page K. L., Osborne J. P., 2022, ATel 15465
- Pagnotta A., et al., 2015, ApJ, 811, 32
- Raj A., et al., 2015, AJ, 149, 136
- Rayner J. T., et al., 2003, PASP, 115, 362
- Rudy R. J., Sitko M. L., Russell R. W., Lynch D. K., 2022, RNAAS, 6, 179
- Rudy R. J., Sitko M. L., Russell R. W., Lynch D. K., 2023, RNAAS, 7, 26
- Ruiter A. J., Ferrario, L., Belczynski K., Seitzzahl I. R., Crocker R. M., Karakas A. I., 2019, MNRAS, 484, 698
- Schaefer B. E., 2010, ApJS, 187, 275
- Schaefer B. E., 2022, MNRAS, 516, 4497
- Shara M. M., Prialnik D., Hillman Y., Kovetz A., 2018, ApJ, 860, 110
- Siviero A., Munari U., 2022, ATel 15417
- Skrutskie M. F., et al., 2006, AJ, 131, 1163
- Sokolovsky K., et al., 2022, ATel 15502
- Starrfield S., Bose M., Iliadis C., Hix W. R., Woodward C. E., Wagner R. M., 2020, ApJ, 895, 70
- Thoroughgood T. D., et al., 2001, MNRAS, 327, 1323
- Tody D., 1986, in Crawford D. L., ed., *Proc. SPIE Conf. Ser. Vol. 627, Instrumentation in Astronomy VI*. SPIE, Bellingham, p. 733
- Tody D., 1993, in Hanisch R. J., Brissenden R. J. V., Barnes J., eds, *Astronomical Society of the Pacific Conference Series, Vol. 52, Astronomical Data Analysis Software and Systems II*, p. 173, Astronomical Society of the Pacific, San Francisco
- Wagner R. M., Depoy D. L., 1996, ApJ, 467, 860
- Williams R. E., Sparks W. M., Gallagher J. S., Ney E. P., Starrfield S., Truran J. W., 1981, ApJ, 251, 221
- Woodward C. E., et al., 2021, ApJ Letters, 922, L10
- Woodward C. E., et al., 2022, ATel 15422
- Yoon S.-C., Langer N., 2005, A&A, 435, 967
- Zombeck M. V., 1990, *Handbook of Astronomy and Astrophysics*, second edition. Cambridge University Press, Cambridge

This paper has been typeset from a \TeX / \LaTeX file prepared by the author.